



Metabolic activity controls the emergence of coherent flows in microbial suspensions

Alexandros A. Fragkopoulos^{ab}, Florian Böhme^a, Nicole Drewes^b, and Oliver Bäumchen^{ab,1}

Edited by Robert Austin, Princeton University, Princeton, NJ; received July 11, 2024; accepted December 16, 2024

Photosynthetic microbes have evolved and successfully adapted to the ever-changing environmental conditions in complex microhabitats throughout almost all ecosystems on Earth. In the absence of light, they can sustain their biological functionalities through aerobic respiration, and even in anoxic conditions through anaerobic metabolic activity. For a suspension of photosynthetic microbes in an anaerobic environment, individual cellular motility is directly controlled by its photosynthetic activity, i.e. the intensity of the incident light absorbed by chlorophyll. The effects of the metabolic activity on the collective motility on the population level, however, remain elusive so far. Here, we demonstrate that at high light intensities, a suspension of photosynthetically active microbes exhibits a stable reverse sedimentation profile of the cell density due to the microbes' natural bias to move against gravity. With decreasing photosynthetic activity, and therefore suppressed individual motility, the living suspension becomes unstable giving rise to coherent bioconvective flows. The collective motility is fully reversible and manifests as regular, three-dimensional plume structures, in which flow rates and cell distributions are directly controlled via the light intensity. The coherent flows emerge in the highly unfavorable condition of lacking both light and oxygen and, thus, might help the microbial collective to expand the exploration of their natural habitat in search for better survival conditions.

microbial motility | metabolic activity | collective behavior | living fluids | photosynthesis

Photoautotrophic microorganisms colonize almost all natural habitats and ecosystems on our planet, by adapting to their frequent and sometimes harsh environmental changes (1). Specifically, spatiotemporal alterations of the light intensity (2, 3) and oxygen (O₂) concentration (4, 5) exert profound effects on the metabolic pathways employed by the cells to produce life-sustaining chemical energy. Even though there exists a diverse set of metabolic pathways, these can generally be grouped into three main categories: photosynthesis, aerobic respiration, and anaerobic fermentation (6). The latter allows for the cells to thrive in a light- and oxygen-depleted environment, termed dark anoxia, (7), which can occur naturally in habitats providing little gas permeability such as soil (8). These conditions can also occur during water eutrophication, where the rapid growth of microorganisms results in the depletion of oxygen in the dissolved water (9, 10).

Understanding and controlling the implications of metabolic pathway switches is not only pivotal for ecological reasons but also for technological applications. Microalgae, and specifically the model organism *Chlamydomonas reinhardtii*, represent microbial systems to produce clean and renewable hydrogen (H₂) (11, 12). While a minor production of H₂ is observed during fermentation (7, 13), the highest yield can be achieved through hydrogenase enzymes during photosynthesis (11, 12, 14). The [Fe/Fe]-hydrogenase HydA1 and HydA2 in *Chlamydomonas* is highly sensitive to O₂, which is a product of photosynthesis, and thus H₂ is naturally inhibited during photosynthesis. As a result, a combination of anoxic conditions with alterations between photosynthesis and darkness seems to attain optimal H₂ production (11, 12, 15).

Metabolic pathway analysis has been used in the study of physiological capacities and features of metabolic networks (16–18). The relation, however, between the metabolic pathways and the cell motility, and by extension the emergence and appearance of collective behavior of a living suspension, remains largely unexplored (19). Self-organized coherent structures in dense microbial suspensions that arises due to the natural tendency of microorganisms to swim against gravity are often summarized under the term “bioconvection”, which is known for depending on the single-cell motility (20–22).

Here, we show that in anaerobic conditions, the spatiotemporal characteristics of coherent flows change and may even reversibly emerge or disappear, depending on the photosynthetic activity of the cells. As a result of the anaerobic conditions, the microbial motility is directly controlled by the light intensity for chlorophyll absorption. Phototactic

Significance

The metabolic activities of photosynthetic microorganisms are of key importance in technological and ecological settings for the capture of carbon dioxide and the transformation of light into chemical energy. Even in the absence of both light and oxygen, microbes may remain motile and sustain metabolic activity capable of synthesizing molecular hydrogen. We found that in such systems, a metabolic switch from photosynthesis to anaerobic respiration induces variations of the single-cell motility that result in the emergence of coherent flows on the population scale. This effect appears to be an adaptation of the microorganisms to their natural habitats and survival strategy in oxygen- and light-deprived environments and has important implications for bioreactor design principles in molecular farming and renewable energy applications.

Author affiliations: ^aExperimental Physics V, Department of Physics, University of Bayreuth, D-95447 Bayreuth, Germany; and ^bMax Planck Institute for Dynamics and Self-Organization, D-37077 Göttingen, Germany

Author contributions: A.A.F. and O.B. designed research; A.A.F., F.B., and N.D. performed research; A.A.F., F.B., N.D., and O.B. analyzed data; and A.A.F. and O.B. wrote the paper.

The authors declare no competing interest.

This article is a PNAS Direct Submission.

Copyright © 2025 the Author(s). Published by PNAS. This open access article is distributed under [Creative Commons Attribution License 4.0 \(CC BY\)](https://creativecommons.org/licenses/by/4.0/).

¹To whom correspondence may be addressed. Email: oliver.baumchen@uni-bayreuth.de.

This article contains supporting information online at <https://www.pnas.org/lookup/suppl/doi:10.1073/pnas.2413340122/-DCSupplemental>.

Published January 23, 2025.

effects, i.e. a biased collective motility in light gradients (23), can be safely ruled out in this scenario through the use of red light and/or photoreceptor (channelrhodopsins) knockout cells (24). The spatiotemporal morphology, cell distributions, and cell circulation rates within the coherent flow structures are regulated by the light intensity, demonstrating a direct link between the activity of metabolic pathways and single-cell as well as collective microbial motility.

Light-Controlled Coherent Flows in Suspensions of Photosynthetic Microbes

Many species within the diverse group of photosynthetic microorganisms perform negative gravitaxis, i.e. exhibit the tendency to move against the gravitational field (25). This form of taxis is essential for their survival, since it allows the cells to increase their chances of locating regions in their environment with more optimal light and aeration conditions. Negative gravitaxis is believed to emerge from the combination of the bottom-heaviness and the shape asymmetry of the cells (25). The term “bottom-heaviness” refers to the inhomogeneous density distribution within a cell, with the chloroplast at the rear of the cell being denser, causing a gravitational torque that aligns the cells against gravity (26). Similarly, the “shape asymmetry” refers to the asymmetric drag force due to the presence of the flagella at the anterior of the cells, causing a similar torque during cell sedimentation (26, 27). Due to negative gravitaxis, the cells tend to form a dense layer at the top surface, with the vertical cell density to theoretically follow an exponential decrease toward deeper regions (28). This inverse sedimentation profile is only stable for sufficiently shallow containers and may become unstable above a critical depth. The latter results in the emergence of distinct bioconvective density patterns (28, 29), as seen in macroscopic experiments, performed in an open Petri dish, shown in Fig. 1A. These bioconvective patterns are stable and display a typical length scale of over 1 mm.

We employ custom-made setups to study suspensions of motile *C. reinhardtii* cells confined in two types of air-tight compartments; see *SI Appendix, Fig. S1A*. First, cylindrical compartments with a diameter of 30 mm and height ranging between

0.5 to 1.0 mm are used to limit edge effects and study the pattern formation in top view; see *SI Appendix, Fig. S1B*. Second, a rectangular cuboid with 30 mm length and 2 mm width and height is used to characterize the coherent flows in side view; see *SI Appendix, Fig. S1C*. The width is sufficiently small to allow the development and observation of single plumes along the width of the compartment. These two compartments will be from now referred to as “3D” and “quasi-2D” compartments. All experiments are performed using red light (wavelength $\lambda = 660 \pm 20$ nm) in order to safely exclude phototactic effects (30) and surface attachment of the cells (31). For consistency the (global) cell density n_0 is kept constant for all experiments at about $8 \cdot 10^7$ cells mL^{-1} . Additionally, we safely ruled out effects of phototaxis by testing double-knockout mutants of channelrhodopsin-1 and -2; see *SI Appendix, Fig. S2*.

When the dense suspension of *C. reinhardtii* cells is exposed to a light intensity of $I = 10^{19}$ photons $\text{m}^{-2} \text{s}^{-1}$, we find that the cells appear homogeneously distributed when viewed from the top; see Fig. 1B, *Right*. By gradually reducing the light intensity, and thus diminishing the photosynthetic activity, the cells are subjected to “self-anaerobization” (19). During this process the cells consume the dissolved O_2 and exhibit short- and long-term changes on the transcription of metabolic enzymes (32), while the boundary conditions inhibit replenishment of the consumed O_2 . We find that under these anaerobic conditions, the same suspension of motile cells forms bioconvection plumes, starting from the edges of the compartment and moving toward the center, until the whole compartment is filled; see Fig. 1B, *Left* and *Middle* and *Movie S1*. Note that even though we expect the oxygen to eventually deplete everywhere (steady state), the rate at which oxygen is depleted depends on the local cell concentration, and thus it will deplete at different rates at different positions in the initial part of the experiment. By using light intensity as a control parameter, we can trigger the formation and disappearance of large-scale coherent flows, and also alter their spatiotemporal morphology. All these effects are completely reversible when reverting the light conditions for the same population of microorganisms.

Even though the microbial suspension at high light intensity appears homogeneous from the top, as discussed, the vertical

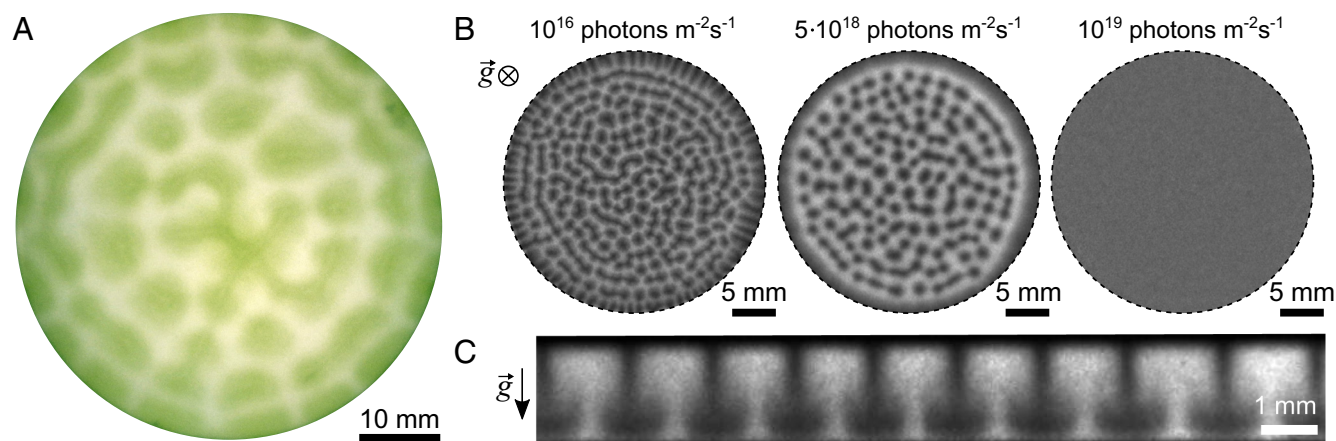


Fig. 1. Light-controlled emergence of coherent flows in living *C. reinhardtii* suspensions. (A) Top-view of a suspension of *C. reinhardtii* under aerobic conditions and homogeneous white light in a Petri dish with cell concentration $n_0 = 8 \cdot 10^7$ cells mL^{-1} and height of the cell suspension 3 mm. (B) Top-view: A suspension of *C. reinhardtii* under anaerobic conditions and red light at different light intensities, confined in an air-tight 3D compartment (height 1 mm, cell concentration $n_0 = 8 \cdot 10^7$ cells mL^{-1}). The suspension displays a homogeneous cell density at high light intensities (*Right*), while convective patterns are observed at reduced light intensities (*Left* and *Middle*). Effects are completely reversible when switching between different light intensities I . (C) Side-view: Structure of the convective rolls of a suspension of *C. reinhardtii* under anaerobic conditions confined in an air-tight quasi-2D compartment ($n_0 = 8 \cdot 10^7$ cells mL^{-1} , $I = 4.6 \cdot 10^{18}$ photons $\text{m}^{-2} \text{s}^{-1}$). See also *Movies S1* and *S2* for the onset of bioconvection in both types of compartments.

distribution of cells is not homogeneous due to negative gravitaxis. To observe modulations of the density along the axis of gravity, we use the side-view imaging offered by the quasi-2D experiments. This setup allows us to quantify the quasi-stationary sedimentation profile at the “homogeneous” (high light intensity) state, and also the spatiotemporal evolution as well as the steady-state of the cell density distributions and flow rates within a plume (low light intensities), as depicted in Fig. 1C and *Movie S2*.

Morphological Characterization of Emergent Light-Controlled Coherent Flows

In order to systematically characterize the emergence and spatiotemporal characteristics of large-scale flow patterns, we perform experiments by first exposing the cell suspension to high light intensity for 10 min to homogenize the density and achieve a quasi-steady state. Afterward, the light intensity is reduced to the desired lower light intensity, and the spatiotemporal evolution of the system is recorded for 15 to 20 min. We then employ a Fourier transform analysis to characterize the evolution of the flow patterns; see *Materials and Methods* for further details.

The peak in the power spectrum $S(q, t)$ corresponds to the most prominent distance within the pattern. By extracting the wavenumber, q_{\max} , that corresponds to this peak, a wavelength can be assigned to the pattern as $\lambda = q_{\max}^{-1}$. This wavelength was measured at different light intensities for both 3D and quasi-2D compartments; see Fig. 2A. In both cases, we do not observe any bioconvection for light intensities $I \geq 10^{19}$ photons $\text{m}^{-2} \text{s}^{-1}$, while bioconvection always occurs for $I \leq 2 \cdot 10^{18}$ photons $\text{m}^{-2} \text{s}^{-1}$. Experiments around $I = 5 \cdot 10^{18}$ photons $\text{m}^{-2} \text{s}^{-1}$ exhibit bistability, with experimental repetitions using the same culture arbitrarily exhibiting bioconvection or the homogeneous state. For 3D compartments, a systematic measure of the wavelengths shows that there is at most a weak dependence of the wavelength on the incident light intensity; see Fig. 2A. However, there is a substantial discrepancy on the values of the wavelengths between the two geometries. For 3D compartments with a height of 1 mm, the wavelength of the bioconvection pattern is $\lambda = 1.7 \pm 0.1$ mm. In the case of the quasi-2D compartment with double the height at 2 mm, the wavelength is measured to be significantly smaller at $\lambda = 1.1 \pm 0.1$ mm. Consequently,

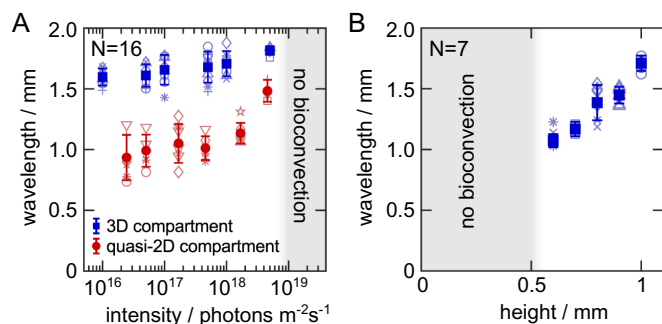


Fig. 2. Light intensity and compartment height control the emergence and appearance of coherent microbial flows. (A) The wavelength of the pattern as a function of the incident light intensity for suspensions with cell concentration $n_0 = 8 \cdot 10^7$ cells mL^{-1} for 3D compartments (blue squares) and quasi-2D compartments (red circles). The height of the compartment is 1 mm. (B) The wavelength of the pattern for 3D compartments as a function of the height of the compartment for a suspension with cell concentration $n_0 = 8 \cdot 10^7$ cells mL^{-1} and light intensity $I = 10^{16}$ photons $\text{m}^{-2} \text{s}^{-1}$. Open symbols indicate technical replicates comprising 1 to 8 repetitions at each light intensity. Filled symbols and their error bar indicate the mean and SD of the N independent biological replicates. Experiments with different light intensities were performed in randomized order.

the confinement of the suspension along one dimension has a profound effect on the fastest unstable mode, such that it is significantly reducing the wavelength of the instability. The wavelength also exhibits a weak dependence on the incident light, except close to the critical light intensity, at which we observe a significant increase.

This confinement effect is further emphasized by analyzing the dependence of the wavelength with the height of the compartment. Fig. 2B shows a monotonic increase of the wavelength of the instability with the compartment height for 3D geometries. This observation is in accordance with previous theoretical work on the subject using no-slip boundary conditions for both surfaces (33). As in previous work, we also observe a critical height below which no convective flows are observed (20, 29). Specifically, in our case, bioconvection never forms for $h \leq 0.5$ mm. Furthermore, experiments at $h = 0.6$ mm are metastable, where bioconvection appears after lowering the light intensity, but always disappears within the course of the experiment.

Now, we use the power spectrum to quantify the temporal dynamics of the pattern formation. More specifically, the temporal evolution of the maximum of power spectrum, $S_{\max}(t)$, is used to measure the dynamic properties of the instability. Since the experiments start in the homogeneous state, $S_{\max}(t)$ has initially a small value. As the instability develops, an initial regime can be identified in which $S_{\max}(t)$ increases exponentially, before it deviates due to nonlinear contributions, and eventually reaches a plateau. An example of $S_{\max}(t)$ in a 3D compartment is shown in *SI Appendix, Fig. S3C*. From these measurements, we identify the onset time, t_{on} , which represents the time required for bioconvection to start after the light intensity is lowered. We find that the onset time is $t_{\text{on}} = 220 \pm 60$ s (from $N = 14$ biological replicates with 64 overall repetitions) and independent of the light intensity; see *SI Appendix, Fig. S4A* for further details. The suspension needs to self-aerobize, i.e. consume all the O_2 within the medium, before bioconvection may be initiated and since we use the same density in the experiments, we expect t_{on} to be constant for our experiments. Finally, we fit the exponential increase after the onset of the instability as $S_{\max}(t) \propto e^{\omega t}$, to extract the growth rate ω , as shown in *SI Appendix, Fig. S3C*. We find that the growth rate $\omega = (4 \pm 2) \cdot 10^{-2} \text{s}^{-1}$ (from $N = 14$ biological replicates with 64 overall repetitions) is independent of the light intensity and also of type of compartment used; see *SI Appendix, Fig. S4B* for further details. Taking these results together we conclude that confinement and light intensity control the appearance, but not the time scales of the evolution of the instability.

Density Distributions and Flow Fields within Coherent Flows

We now systematically characterize the effect of light intensity on the cell density distributions and the cell flow organization within plumes in the quasi-steady state. By applying Eq. 15 derived in *Materials and Methods*, we estimate the relative cell density within stable bioconvective plumes at different light intensities based on the quasi-2D experiments. We observe that the cell distribution changes significantly at different light conditions, with the center of the plume (region of highest cell density) progressively moving upward with increasing light intensity, as depicted in Fig. 3A. We also observe that the range of relative cell densities becomes narrower as the light intensity increases. Specifically, the highest observed relative cell density at $I = 1.7 \cdot 10^{17}$ photons $\text{m}^{-2} \text{s}^{-1}$ is $(n - n_0)/\alpha \approx 0.4$, while at $I = 4.6 \cdot 10^{18}$ photons $\text{m}^{-2} \text{s}^{-1}$

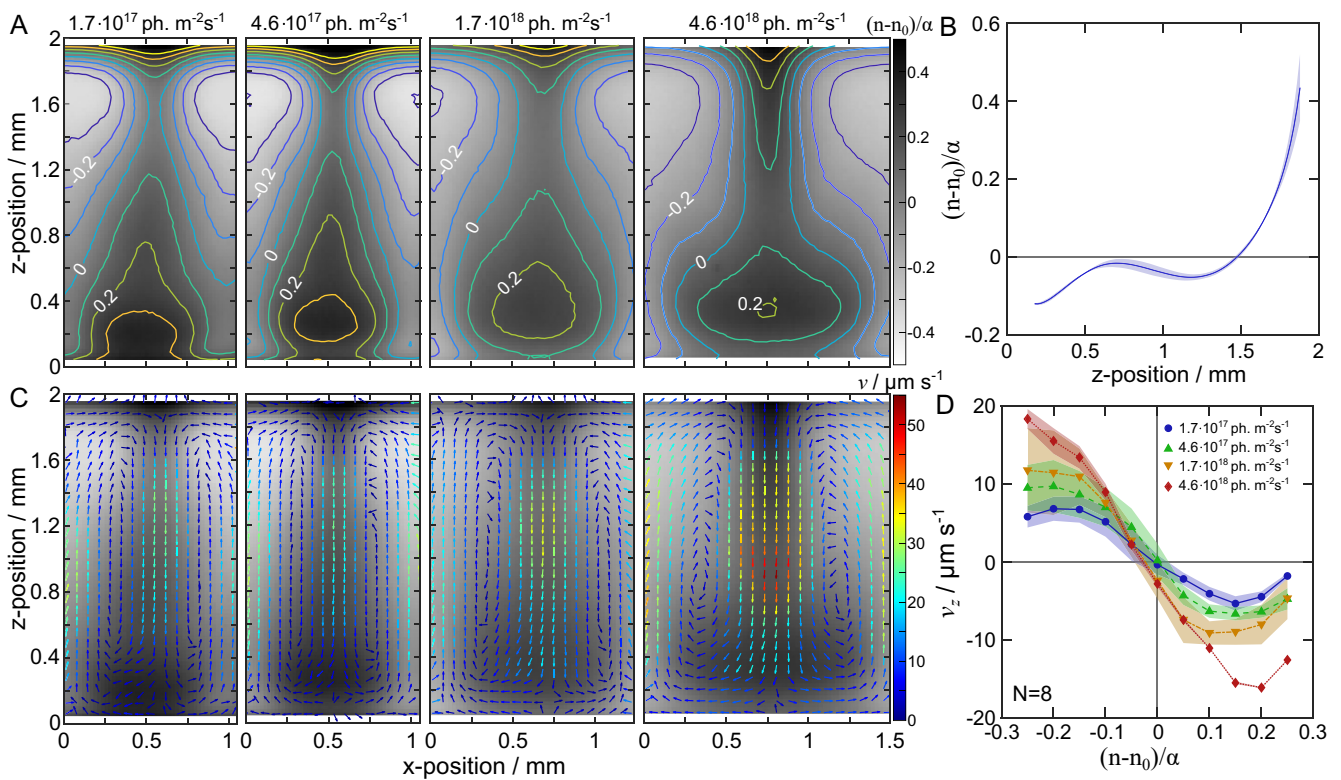


Fig. 3. Density distribution and cell flow organization within plumes in *C. reinhardtii* suspensions. (A) Vertical cross-sections of the relative cell density $(n - n_0)/\alpha$ of stable bioconvective plumes at different light intensities. Contour lines represent the isolines for relative cell densities $(n - n_0)/\alpha$. (B) Inverse sedimentation profile: The relative cell density $(n - n_0)/\alpha$ at high light intensity ($I = 4.6 \cdot 10^{19}$ photons $m^{-2} s^{-1}$) is plotted as a function of the z -coordinate with respect to the bottom of the container. At this light intensity, the suspension exhibits an inverted sedimentation profile and no coherent flows. (C) Flow velocity fields within stable bioconvective plumes are measured using Particle Image Velocimetry (PIV) for the experiments and light intensities displayed in panel (A). (D) Velocity-density coupling: The vertical component of the cell flow, v_z , is displayed as a function of the relative cell density $(n - n_0)/\alpha$ for the flow velocity fields displayed in panel (C). The value of v_z is given as the average vertical velocity for the same density $(n - n_0)/\alpha$ with a bin size of 0.5, with a positive v_z indicating an upward cell flow. All data are for cell suspensions in a quasi-2D compartment with an average cell density $n_0 = 8 \cdot 10^7$ cells mL^{-1} . Filled symbols and their error indicate the mean and SD of N independent biological replicates. Experiments with different light intensities were performed in randomized order. The data for $I = 4.6 \cdot 10^{18}$ photons $m^{-2} s^{-1}$ exhibit less statistics, since this corresponds to the threshold between inverse sedimentation and bioconvection, with only one biological replicate showing bioconvection with three technical replicates.

is $(n - n_0)/\alpha \approx 0.2$. At sufficiently high light intensity the bioconvection disappears, and an inverse sedimentation profile is instead acquired, as shown in Fig. 3B.

Complementary to the experimental quantification of cell density distributions, we also established particle image velocimetry (PIV) methods to measure the flow of cells within the plumes (34). Conventional PIV entails that a fluid is seeded with tracer particles and consecutive images of the flow with the particles are correlated in order to measure the local fluid flow. Here, we use the cells as the tracer particles, which due to the self-propelled nature of the cells do not necessarily follow the flow of the surrounding fluid. Thus, we rather measure the cell flow, which is the combination of the fluid flow coupled with the average motility of the cells with respect to the surrounding fluid.

For all light intensities, we observe that the cells accumulate in regions of downwelling flow, while the relative density is substantially reduced in regions of upwelling flow as compared to the global cell density; see Fig. 3C. This is expected due to gyrotactic effects. The combination of the gravitactic torque, which aligns the cells against gravity, and the viscous torque, which is the result of the nonzero vorticity field, cause the cells to orient towards, and thus accumulate in, regions of downwelling flows, a phenomenon known as gyrotaxis (35). For different light intensities, the circulation rates increase with increasing

light intensity, with the maximum cell flow velocity rising from $25 \mu m s^{-1}$ to $55 \mu m s^{-1}$. These findings are in line with a higher motility of the microbes on the single-cell level at higher light intensities under anaerobic conditions, which will be discussed in more detail in the following paragraph.

To further quantify these effects on the population scale, we measure the average vertical cell flow, v_z , in regions of comparable cell density as a function of the local cell density, as shown in Fig. 3D. We observe the gyrotactic accumulation of cells in regions of downwelling flow, which manifests as the negative correlation between the vertical component of the cell flow and the cell density. Finally, a faster turnover of the cell flow is observed at high light intensities, with the maximum circulation velocity increasing from $8 \mu m s^{-1}$ to $19 \mu m s^{-1}$ with increasing light intensity.

Effect of Metabolic Activity on the Single-Cell Motility

Linking the emergence and appearance of coherent flows to the activity of the individual constituents requires a quantitative understanding of the cell motility and its connection to the microbial metabolism. The motion of *C. reinhardtii* can be modeled as a run-and-tumble (RT) motility (36), where the cells exhibit short-time ballistic motion (run) that is interrupted by sudden

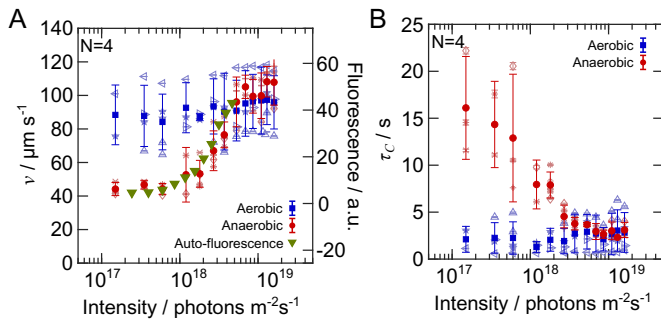


Fig. 4. Effect of the photosynthetic activity on the single-cell motility. (A) The RMS velocity, v , and (B) the velocity correlation time, τ_c , of the cells as a function of light intensity under aerobic (blue circles) and anaerobic (red squares) conditions. Multiple experiment were performed at different cell densities, ranging between 500 to 1,300 cells mm^{-2} . (A) Chlorophyll autofluorescence (green triangles) as a function of the light intensity represents a proxy of the photosynthetic activity of the cells and correlates well with the cell velocity in anaerobic conditions (red squares). See *Materials and Methods* for further details. Experiments were performed in compartments with a height of $h = 25 \mu\text{m}$ in order to confine the motility of the cell to 2D. For each biological replicate, the trajectories of 1,500 to 4,500 cells were recorded and were used to calculate v and τ_c . Open symbols indicate technical replicates comprising 1 to 3 repetitions at each light intensity. Filled symbols and their error bar indicate the mean and SD of the N independent biological replicates. Experiments with different light intensities were performed in randomized order.

reorientations (tumble). The motility can be quantified using the velocity autocorrelation function (37), $C_v(t) = \langle \mathbf{v}_i(t=0) \cdot \mathbf{v}_i(t) \rangle$, where the average is taken over all tracked cells with \mathbf{v}_i representing the velocity of the i th individual cell. These experiments are performed in compartments with a height of $25 \mu\text{m}$ following the protocol outlined in ref. 19. In order to dissect the effect of the microbial metabolism, experiments are performed under aerobic (air-permeable compartments) and anaerobic (airtight compartments) conditions, while monitoring the photosynthetic activity using the chlorophyll autofluorescence signal as a proxy.

The velocity autocorrelation C_v follows an exponential decay in all cases (SI Appendix, Fig. S5) and can be expressed as $C_v = v^2 e^{-t/\tau_c}$, where $v = \sqrt{\langle v^2 \rangle}$ is the root-mean square (RMS) velocity, and τ_c denotes the velocity correlation time (19). In aerobic conditions, the motility is independent of the light intensity with $v = 92 \pm 16 \mu\text{m s}^{-1}$ and $\tau_c = 2.4 \pm 1.7 \text{ s}$, as shown in Fig. 4 A and B. In contrast, the motility of the cells directly depends on the light conditions in the case of anaerobic conditions, i.e. the RMS velocity v monotonically decreases while the velocity correlation time τ_c increases with decreasing light intensity, respectively. These values eventually reach a plateau at $v = 46 \pm 3 \mu\text{m s}^{-1}$ and $\tau_c = 15 \pm 5 \text{ s}$ for $I < 7 \cdot 10^{17} \text{ photons m}^{-2} \text{ s}^{-1}$. For light intensities $I \geq 7 \cdot 10^{18} \text{ photons m}^{-2} \text{ s}^{-1}$, the motility of the cells is consistent with its values obtained for aerobic conditions. At the same time, we observe that the chlorophyll autofluorescence increases with the incident light intensity in the range of intensities where the cell motility changes, as depicted in Fig. 4A. Furthermore, the chlorophyll autofluorescence plateaus to a minimum for $I < 7 \cdot 10^{17} \text{ photons m}^{-2} \text{ s}^{-1}$, which is in line with the cell motility.

In summary, single-cell motility assays together with measurements of the chlorophyll autofluorescence of the microbes demonstrate that under anaerobic conditions, the photosynthetic activity directly controls the motility of the cells and thus appears to be responsible for the emergence of coherent flows in such light-regulated living fluids.

Discussion

To understand how rather subtle changes of individual microbial motility may induce or suppress population-scale convective instabilities in living fluids, we briefly revisit the state-of-the-art theoretical background for bioconvection. Continuum theories of gyrotactic organisms use the following equations to describe the system:

$$\text{incompressibility: } \nabla \cdot \mathbf{u}_f = 0, \quad [1]$$

$$\text{momentum: } \frac{D\mathbf{u}_f}{Dt} = -\nabla p_f + \nu \Delta \mathbf{u}_f + n v_c \Delta \rho \mathbf{g}, \quad [2]$$

$$\text{gyrotaxis: } \frac{\partial \mathbf{p}}{\partial t} = \frac{1}{2B} (\hat{\mathbf{e}}_z - (\hat{\mathbf{e}}_z \cdot \mathbf{p}) \mathbf{p}) + \frac{1}{2} \boldsymbol{\omega} \times \mathbf{p}, \quad [3]$$

$$\text{cell conservation: } \frac{\partial n}{\partial t} = -\nabla \cdot (n \mathbf{u}_f + n v \mathbf{p} - D \nabla n), \quad [4]$$

where \mathbf{u}_f is the velocity of the fluid, p_f the fluid pressure, ν the kinematic viscosity, v_c the volume of a single cell, $\Delta \rho = \rho_c - \rho$ with ρ_c and ρ the mass density of the cell and the fluid respectively, \mathbf{g} the gravitational acceleration, B the time for a cell to orient with gravity due to gravitaxis, \mathbf{p} the average cell orientation, $\boldsymbol{\omega} = \nabla \times \mathbf{u}_f$ the vorticity, v the average cell speed, and D the diffusion constant of the cells (28, 38). Using Eqs. 1–4, the following dimensionless numbers characterize the system:

$$\text{bioconvective Rayleigh number: } R = \frac{g \phi \Delta \rho h^3}{\rho \nu D}, \quad [5]$$

$$\text{scaled cell speed: } w = \frac{v h}{D}, \quad [6]$$

$$\text{gyrotactic number: } G = \frac{B D}{b^2}, \quad [7]$$

$$\text{Schmidt number: } Sc = \frac{\nu}{D}, \quad [8]$$

where $\phi = n_0 v_c$ is the volume fraction of the suspension, and h the height of the compartment (28). Similar to the classical Rayleigh-Bénard instability in a nonliving fluid, the suspension is unstable and thus is expected to be prone to bioconvective instabilities above a critical Rayleigh number, i.e. for $R > R_c(w, G, Sc)$.

In the following, we derive the relevant dimensionless numbers specifically for our system of photoactive microbes. We retrieve the diffusion constant D of the cells by using the velocity autocorrelation functions as

$$D = \frac{1}{d} \int_0^\infty C_v(t) dt, \quad [9]$$

where d is the dimensionality of the system (39). Since the experiments were performed in a quasi-2D environment, the diffusion constant is given as $D = v^2 \tau_c / 2$, provided C_v follows the exponential form. Even though both v and τ_c change with light under anaerobic conditions; see Fig. 4, we find that D remains largely independent of the light intensity with a value of $D = (1.6 \pm 0.5) \cdot 10^4 \mu\text{m}^2 \text{ s}^{-1}$. As a result R , G , and Sc are constant for the different light intensities, with only the scaled velocity w increasing substantially from 5.8 to 11.5 with increasing light intensity. We find the Rayleigh number $R = 640$ for the 3D experiments using the corresponding values of $g = 9.8 \text{ m s}^{-2}$, $\phi = 2.1\%$, $\Delta \rho / \rho = 0.05$ (40), $h = 1 \text{ mm}$, $\nu = 10^{-6} \text{ m}^2 \text{ s}^{-1}$, and $D = 1.6 \cdot 10^4 \mu\text{m}^2 \text{ s}^{-1}$.

Since for this type of living fluid R is a constant, the only way for the suspension to reversibly switch between stable and unstable conditions is a change of the critical Rayleigh number, R_c , between light intensities. The system exhibits constant G and S_c , and thus R_c may only change if w changes. For suspensions exhibiting a finite depth with $w > 1$, no-slip boundary conditions, and an initial inverted sedimentation profile, as in our case, $R_c \propto w^4$ (28). Consequently, the value of R_c is reduced by a factor of 15 between the high and low light intensities in our photoactive living fluid. As the light intensity and, thus, w decrease, R_c decreases to the point that the Rayleigh number of the system becomes larger than its critical value, i.e. $R > R_c$. As a result, the suspension becomes unstable initiating the global formation of bioconvective flows. Theoretically, the fastest unstable mode, which determines the wavelength of the pattern, is almost independent of w (28), in agreement with our experimental observations. Unfortunately, we cannot explicitly calculate the theoretical values of R_c and the wavelength at different light intensities, since B remains unknown. It is important to note that this theoretical approach has some limitations, since Eq. 3 ignores reorientations of the cells due to tumbles and the effect of cell–cell interactions, while in Eq. 4 the values of v and D are not constant, but they are rather density-dependent due to cell–cell interactions (19).

This mechanism is further supported by simulations of bottom-heavy active Brownian particles including steric as well as hydrodynamic interactions, where the active suspension is found to transition from an inverted sedimentation to plumes and finally to regular sedimentation with decreasing particle velocity (41). However it needs to be noted that in this numerical work (41), the relative size of cells and compartment height differ from our experiments, and the plumes observed are not stable but rather transient states. Our recommendation to describe the system is to use overdamped stochastic Langevin equations for the motility of a single cell including the different cell interactions:

$$\text{position : } \frac{d\mathbf{r}_c}{dt} = \mathbf{u} \hat{e}_c + \frac{1}{\zeta_t} (\mathbf{F}_{\text{steric}} + \mathbf{F}_{\text{hydr}}), \quad [10]$$

$$\text{orientation : } \frac{d\hat{e}_c}{dt} = \boldsymbol{\xi} + \frac{1}{\zeta_r} (\mathbf{T}_{\text{steric}} + \mathbf{T}_{\text{hydr}}), \quad [11]$$

where \mathbf{r}_c and \hat{e}_c are the position and orientation of a single cell, \mathbf{u} the velocity of a cell in the absence of interactions, ζ_t and ζ_r are the translational and rotational friction coefficients, $\mathbf{F}_{\text{steric}}$, \mathbf{F}_{hydr} the forces and $\mathbf{T}_{\text{steric}}$, \mathbf{T}_{hydr} the torques due to steric and hydrodynamic interactions, respectively, and $\boldsymbol{\xi}$ is a white noise term, such that $\langle \xi_i(t) \xi_j(t') \rangle = 2D_r \delta_{ij} \delta(t - t')$ with D_r the rotational diffusion constant of the cells.

In contrast to our experiments, previous work has exclusively focused on aerated suspensions with an air–liquid interface. In that case, variation of the illumination intensity of red light does neither alter the formation nor the morphology of the bioconvection patterns for *Chlamydomonas augustae*, a similar photosynthetic microorganism (29). For *C. reinhardtii* a reduction of red-light intensity using intermittent short-time exposure to light pulses has been reported to not show an immediate change of the bioconvective pattern, even though such periodic illumination is found to alter long-term pattern rearrangements (42). Here, we use continuous illumination in anaerobic conditions and show that the emergence and disappearance of bioconvective patterns are reversibly switchable by light.

Conclusion

We reveal the effect of the metabolism on the individual as well as the collective microbial motility. Under aerobic conditions, the motility of photosynthetically active microbes remains unaffected by the intensity of the incident light, since cells access oxygen enabling them to perform aerobic respiration. In contrast, the cell motility exhibits drastic changes with decreasing light intensity under anaerobic conditions, providing a unique control parameter for the microbial motility in the complete absence of phototaxis. The changes of the metabolic activity and the motility of individual cells exert profound effects on the population dynamics. Due to the natural tendency of the cells to move against gravity, the living suspension exhibits a stable inverse sedimentation profile at high light intensities, but develops coherent flows as the light intensity decreases sufficiently for the single-cell motility to be altered. In this system, light provides direct experimental access to the impact of microbial motility on bioconvective flows. In line with previous analytical as well as numerical work, a decrease of the cell velocity induces the manifestation of bioconvective patterns. The physical mechanism behind this phenomenon bases on the microbes' preference to accumulate at the top interface at high light intensity and propulsion velocity due to their dominant bottom heaviness and thus upward orientation during swimming. On the population scale, this effect causes an inverted sedimentation profile within the living suspension. As the propulsion velocity decreases substantially with lowered photosynthetic activity, and thus adenosine triphosphate (ATP) synthesis rates, the gravitational force exceeds the net upward propulsion, causing the cells at the top interface to sediment. In turn, gyrotaxis effects cause the cells to accumulate in highly localized downwelling flows, finally leading to the emergence of spatially regular and temporally stationary bioconvective plumes.

In summary, confined photosynthetically active microbial suspensions display reversibly light-switchable coherent flows. For unfavorable natural conditions in which—at least locally and temporally—both oxygen and light may be deprived, this mechanism might be advantageous for the survival and propagation of the entire microbial community. In technological settings involving, e.g., the synthesis of molecular hydrogen, the findings may guide design principles for photobioreactors in the fields of renewable energies and molecular farming.

Materials and Methods

Cell Cultivation. Wild-type *C. reinhardtii* cells, strain SAG 11-32b provided by the Göttingen Algae Culture Collection (SAG, Göttingen, Germany), were grown axenically in Tris-Acetate-Phosphate (TAP, Gibco™) medium on 12 h-12 h day-night cycles at temperatures of 24 °C and 22 °C, respectively, in a Memmert IPP260ecoplus incubator. Cultures of 100 mL were prepared in 250 mL Erlenmeyer flasks and placed on an orbital shaker (Advanced Mini Shaker 15, VWR) with an orbit diameter of 15 mm at 100 rpm. The daytime light intensity in the incubator was (1 to 2) · 10¹⁹ photons m⁻² s⁻¹ using cool white (6,500 K) LEDs, and zero during the nighttime. Vegetative cells were taken from the cultures in the logarithmic growth phase during the daytime on the third or fourth day after starting the incubation. In order to increase the cell density, the culture was centrifuged for 10 min at an acceleration of 100 g, the excess fluid was removed, and the pellet of cells was resuspended in fresh TAP medium. Since cells may deflagellate due to the mechanical stress during the centrifugation, the cell suspension was allowed to rest for 1.5 h to allow for regrowing their flagella (40). A hemocytometer (Neubauer-improved with double net ruling) was used to manually measure the cell density, and then dilute the suspension to the final desired density of (8 ± 1) · 10⁷ cells/mL.

Bioconvection Setup. All bioconvection experiments were performed with a custom-made setup. The imaging of the samples was either performed in horizontal or vertical orientation depending on the type of compartment used; see *SI Appendix, Fig. S1*. The experiments were performed under red light to exclude both phototaxis (30) and adhesion to surfaces (31, 43). An light-emitting diode (LED) light source with center wavelength of 660 nm and a full width at half maximum (FWHM) of 20 nm was used to illuminate the sample (M660L4, Thorlabs). An optical diffuser was used to homogenize the light from the light source (DG20-600, Thorlabs), while neutral density filters with optical densities of 1 or 2 were used to expand the range of light intensities that can be used in the experiment (NE2R10B and NE2R20B, Thorlabs). A condenser lens was used to ensure Köhler illumination, which provides reproducible and homogeneous illumination conditions (LA1740, Thorlabs). The image is focused using a macro-zoom lens (12.5 to 75 mm f1.8, Avenir, Japan) and recorded at 3 fps with a CMOS camera (Grasshopper3, GS3-U3-51S5M, Flir) with an 8-bit depth. The camera sensor has a size of $2,448 \times 2,048$ pixels with a pixel size of 3.45 μm . For both experimental configurations (bioconvection and cell motility setup) the light intensity was calibrated using a Thorlabs PM100D powermeter (Thorlabs S130C photodiode power sensor) for monochromatic light.

The compartments for containing the living suspensions were made of custom-made stainless steel parts in between two soda lime glass slides (Marienfeld Superior), as shown in *SI Appendix, Fig. S1 Band C*. In order to ensure that the compartments are airtight, the parts were manually clamped together. Functionalizing the glass slides with a thin polydimethylsiloxane (PDMS) coating has shown to improve the sealing with the steel component. For this coating, Sylgard 184 PDMS (Dow Chemical) was mixed with a 10:1 by weight ratio of base to curing agent. The mixture of PDMS was spin-coated using a commercial spin-coater (WS-650MZ-23NPPB, Laurell Technologies Corp., US) onto a glass slide at 950 rpm for 5 min, to achieve the final thickness of about $21 \pm 1 \mu\text{m}$. After spin-coating, the glass slide was immediately placed on a hot plate for 4 min at about 95 °C to accelerate the cross-linking process. Afterward, the glass slides were placed in an oven at 75 °C for 2 h to complete the polymerization process. Since the PDMS coating renders the glass surface hydrophobic, it impedes the filling of the compartments with the suspension without air bubbles. For this reason, the coated glass slides are plasma cleaned with atmospheric air for 30 s (Atto plasma cleaner, Diener, Germany), which renders the surface hydrophilic. All data provided in Fig. 3 in quasi-2D compartments were obtained for light intensities $I \geq 1.7 \cdot 10^{17}$ photons $\text{m}^{-2} \text{s}^{-1}$. For lower light intensities, bioconvective plumes in the quasi-2D compartments did emerge but not achieve a clear steady state.

The experiments for bioconvection in aerobic conditions, shown in Fig. 1A, were performed using conventional polystyrene petri dishes with a 55 mm inner diameter (VWR). The petri dishes were plasma cleaned with atmospheric air for 30 s to render the surface hydrophilic, after which the cell suspension was carefully pipetted in. Finally, the suspension was illuminated with a halogen cold light source (LK 1500 LCD, Schott).

Cell Motility Setup. The cell motility experiments were performed using an Olympus IX81 inverted microscope. The condenser was always adjusted to ensure Köhler illumination. An interference bandpass filter with center wavelength of 671 nm and a FWHM of 10 nm ensured consistent illumination of the sample with red light in these experiments. A $4\times$ objective was used in conjunction with the magnification changer set at $1.6\times$ resulting to a total of $6.4\times$ magnification. Videos were recorded at 30 fps with a CMOS camera (Grasshopper3, GS3-U3-41C6M, Flir).

The airtight compartments are the same as the 3D compartments, shown in *SI Appendix, Fig. S1B*, but with a height of 25 μm and a 3 mm diameter. The air-permeable compartments were made using the spin-coated PDMS of a height of $21 \pm 1 \mu\text{m}$ as described in the previous sections. A 3 mm in diameter circular punch (Harris Uni-Core) was used to produce the desired circular compartment. In addition, the top glass slide was exchanged for a 1 mm thick solid PDMS to allow for sufficient air exchange.

The circular Hough transform was used to detect the cells (44), which requires only partial detection of the cell's edge to identify it. The circular Hough transform requires a previous knowledge of the radius of the cells. In our case, we used a range of radii between 2.6 μm and 5.5 μm (43). The trajectories of the detected

cells are determined using a Matlab-based code by Blair and Dufresne (45), which requires the maximum distance that cells can be displaced between consecutive frames. We chose this parameter to be 7 μm , which results in a maximum instantaneous velocity of 233 $\mu\text{m s}^{-1}$. Finally, the cell velocity is calculated as the displacement of the tracked cells over one frame.

Fourier Analysis and Particle Imaging Velocimetry. Since the wavelength of the instability rarely matches exactly the discretization of the gathered data, spectral leakage occurs, where the peak of the power spectrum leaks into nearby wavelengths (46). To limit this effect, we scale the intensity in our images, $J(x, z, t)$, with the Hamming window, $H(x, z)$ (47). The resultant power spectrum is given as:

$$S(q_x, q_y, t) = \frac{|\mathcal{F}[J(x, y, t) \cdot H(x, y)]|}{|\mathcal{F}[H(x, y)]|}, \quad [12]$$

where \mathcal{F} is the Fourier transform operator, while q_x and q_y are the wavenumbers along the horizontal and vertical directions of the images. In the case of the 3D compartments, $S(q_x, q_y, t)$ exhibits azimuthal symmetry; see *SI Appendix, Fig. S3A* for a representative example. Consequently, we use the azimuthal average for our analysis, i.e. $S(q, t) = \langle S(q_x, q_y, t) \rangle_\theta$, where θ is the azimuthal angle. An example of $S(q, t)$ in a 3D compartment is provided in *SI Appendix, Fig. S3B*. Due to the limited height in quasi-2D compartments, we use instead a 1D signal for the Fourier transform along the length of the compartment. The images, $J(x, z)$, were first converted to a 1D signal as $J(x) = \langle J(x, z) \rangle_z$. Using this 1D signal the same process as in Eq. 12 was performed using a 1D Hamming window.

For the PIV analysis, the Matlab-based and open access software PIVlab was used (48). The images are preprocessed using an enhanced local contrast algorithm, specifically the contrast limited adaptive histogram equalization algorithm (CLAHE), with a window size of 1.5 mm (49). The images were analyzed using the fast Fourier transform window deformation algorithm with progressive refinement of the interrogation window size (0.24, 0.19, 0.15 mm) and step size (0.12, 0.1, 0.7 mm). Finally, we average the cell flow field over all the processed frames of the stable plume.

Cell Density Estimation. To quantify the cell density, we use the Beer-Lambert law that estimates the concentration of light-absorbing matter by measuring the attenuation of light (50). Specifically, the Beer-Lambert law is given by

$$n = -\alpha \log \left(\frac{I_T}{I_0} \right), \quad [13]$$

where ρ is the local cell density, and I_T and I_0 the transmitted and incident light intensity, respectively. The parameter α depends solely on the path length of the light and the attenuation coefficient of the cells. Since all quasi-2D experiments exhibit equivalent width, thus the same path length, α can be considered a constant for these experiments. During experiments, we measure the transmitted light intensity I_T , and thus two parameters in Eq. 13 remain unknown, namely α and I_0 . Since we perform all experiments with the same cell density, we leverage this to reduce the number of unknown parameters. Given Eq. 13, we can calculate the average cell density as

$$n_0 = \frac{1}{A} \iint_A n \, dx \, dz = -\alpha \left\langle \log \left(\frac{I_T}{I_0} \right) \right\rangle, \quad [14]$$

where A is the area over which we view the suspension. Using Eqs. 13 and 14 and that I_0 is considered a constant within the processed area, we estimate the relative cell density in the sample as

$$\left(\frac{n - n_0}{\alpha} \right) = \langle \log(I_T) \rangle - \log(I_T). \quad [15]$$

The Beer-Lambert law is based on the absorption of light, and it does not take into account light scattering. Even though it provides a good approximation of the cell density (50), it deviates at high cell densities, where scattering becomes prominent. This transition is shifted to higher cell densities in the case of photosynthetic organisms specifically due to the high absorbance capacity of photosynthetic pigments at specific wavelengths as is in our case (51). Nevertheless, we note that using this method might result in an underestimation of the cell density in dense regions.

Chlorophyll Autofluorescence. Chlorophyll a/b exhibit two major peaks of absorption around 470 nm and 670 nm, while they emit light at higher wavelengths in the range of 650 to 750 nm via autofluorescence (52). Autofluorescence measurements were performed along the line of the cell motility experiments using a spin-coated PDMS compartment with a glass slide cover. In these experiments, a 671 nm bandpass filter with a 10 nm FWHM was placed between the light source and the sample, while a 700 nm long-pass filter right after the sample allows only the fluorescent light to be detected by the camera. For consistency, the camera settings were kept constant for all experiments. Two experimental measurements were performed for each light intensity: one with the sample and one without. Each measurement consisted of a series of 300 images captured at 33 fps using a sCMOS camera (Iris 9, Photometrics) with relatively high quantum efficiency (~66% in red light) and 16-bit depth. The camera sensor has a size of 2,960 × 2,960 pixels with a pixel size of 4.25 μm. Images acquired without any sample were used to

subtract the background noise in the actual measurements. Finally, the average autofluorescence signal was then calculated for each light intensity, which is displayed in Fig. 4C.

Data, Materials, and Software Availability. Raw data underlying data presented in the figures have been deposited in Zenodo (53).

ACKNOWLEDGMENTS. We sincerely thank the Göttingen Algae Culture Collection (SAG) for providing the *C. reinhardtii* wild-type strain SAG 11-32b and Peter Hegemann (Humboldt University of Berlin) for providing the channelrhodopsin-1,2 double knockout mutant (CC-5679) in this background. We thank M. Lorenz, S. Herminghaus, M. Wilczek, C.-M. Koch, and H. Stark for stimulating scientific discussions and K. Oetter for technical assistance. Funding from the Max Planck Society is acknowledged.

- J. A. Raven, R. J. Geider, "Adaptation, acclimation and regulation in algal photosynthesis" in *Photosynthesis in Algae*, A. W. D. Larkum, S. E. Douglas, J. A. Raven, Eds. (Springer, 2003), pp. 385–412.
- K. K. Singh, R. Shyam, P. V. Sane, Reactivation of photosynthesis in the photoinhibited green alga *Chlamydomonas reinhardtii*: Role of dark respiration and of light. *Photosynth. Res.* **49**, 11–20 (1996).
- X. Xue, D. A. Gauthier, D. H. Turpin, H. G. Weger, Interactions between photosynthesis and respiration in the green alga *Chlamydomonas reinhardtii* (characterization of light-enhanced dark respiration). *Plant Physiol.* **112**, 1005–1014 (1996).
- A. Atteia, R. van Lis, A. G. Tielens, W. F. Martin, Anaerobic energy metabolism in unicellular photosynthetic eukaryotes. *Biochim. Biophys. Acta* **1827**, 210–223 (2013).
- W. Yang, C. Catalanotti, T. M. Wittkopp, M. C. Posewitz, A. R. Grossman, Algae after dark: Mechanisms to cope with anoxic/hypoxic conditions. *Plant J.* **82**, 481–503 (2015).
- A. R. Grossman, F. A. Wollman, *The Chlamydomonas Sourcebook: Volume 2: Organellar and Metabolic Processes* (Academic Press, 2023).
- F. Mus, A. Dubini, M. Seibert, M. C. Posewitz, A. R. Grossman, Anaerobic acclimation in *Chlamydomonas reinhardtii*: Anoxic gene expression, hydrogenase induction, and metabolic pathways. *J. Biol. Chem.* **282**, 25475–25486 (2007).
- F. Garcia-Pichel, J. Belnap, "Small-scale environments and distribution of biological soil crusts" in *Biological Soil Crusts: Structure, Function, and Management*, J. Belnap, O. L. Lange, Eds. (Springer, 2003), pp. 193–201.
- D. M. Anderson, P. M. Glibert, J. M. Burkholder, Harmful algal blooms and eutrophication: Nutrient sources, composition, and consequences. *Estuaries* **25**, 704–726 (2002).
- P. M. Glibert, Eutrophication, harmful algae and biodiversity-challenging paradigms in a world of complex nutrient changes. *Mar. Pollut. Bull.* **124**, 591–606 (2017).
- M. G. Esquivel, H. M. Amaro, T. S. Pinto, P. S. Feveireiro, F. X. Malcata, Efficient H₂ production via *Chlamydomonas reinhardtii*. *Trends Biotechnol.* **29**, 595–600 (2011).
- G. Torzillo, A. Scoma, C. Faraloni, L. Giannelli, Advances in the biotechnology of hydrogen production with the microalga *Chlamydomonas reinhardtii*. *Crit. Rev. Biotechnol.* **35**, 485–496 (2015).
- R. P. Gfeller, M. Gibbs, Fermentative metabolism of *Chlamydomonas reinhardtii*: I. Analysis of fermentative products from starch in dark and light. *Plant Physiol.* **75**, 212–218 (1984).
- M. Forestier *et al.*, Expression of two [Fe]-hydrogenases in *Chlamydomonas reinhardtii* under anaerobic conditions. *Eur. J. Biochem.* **270**, 2750–2758 (2003).
- C. R. Williams, M. A. Bees, Mechanistic modeling of sulfur-deprived photosynthesis and hydrogen production in suspensions of *Chlamydomonas reinhardtii*. *Biotechnol. Bioeng.* **111**, 320–335 (2014).
- T. Cakir *et al.*, Integration of metabolome data with metabolic networks reveals reporter reactions. *Mol. Syst. Biol.* **2**, 50 (2006).
- J. O. Krömer, C. Wittmann, H. Schröder, E. Heinzle, Metabolic pathway analysis for rational design of l-methionine production by *Escherichia coli* and *Corynebacterium glutamicum*. *Metab. Eng.* **8**, 353–369 (2006).
- P. Unrean, F. Srien, Metabolic networks evolve towards states of maximum entropy production. *Metab. Eng.* **13**, 666–673 (2011).
- A. A. Fragkopoulou *et al.*, Self-generated oxygen gradients control collective aggregation of photosynthetic microbes. *J. R. Soc. Interface* **18**, 20210553 (2021).
- N. Hill, T. Pedley, Bioconvection. *Fluid Dyn. Res.* **37**, 1 (2005).
- A. Sengupta, F. Carrara, R. Stocker, Phytoplankton can actively diversify their migration strategy in response to turbulent cues. *Nature* **543**, 555–558 (2017).
- M. A. Bees, Advances in bioconvection. *Annu. Rev. Fluid Mech.* **52**, 449–476 (2020).
- J. Dervaux, M. Capellazzi Resta, P. Brunet, Light-controlled flows in active fluids. *Nat. Phys.* **13**, 306–312 (2017).
- O. A. Sineshchekov, K. H. Jung, J. L. Spudich, Two rhodopsins mediate phototaxis to low- and high-intensity light in *Chlamydomonas reinhardtii*. *Proc. Natl. Acad. Sci. U.S.A.* **99**, 8689–8694 (2002).
- A. Roberts, Mechanisms of gravitaxis in *Chlamydomonas*. *Biol. Bull.* **210**, 78–80 (2006).
- A. Kage, T. Otori, K. Kikuchi, T. Ishikawa, The shape effect of flagella is more important than bottom-heaviness on passive gravitactic orientation in *Chlamydomonas reinhardtii*. *J. Exp. Biol.* **223**, jeb205989 (2020).
- A. Roberts, F. Deacon, Gravitaxis in motile micro-organisms: The role of fore-aft body asymmetry. *J. Fluid Mech.* **452**, 405–423 (2002).
- N. Hill, T. Pedley, J. O. Kessler, Growth of bioconvection patterns in a suspension of gyrotactic micro-organisms in a layer of finite depth. *J. Fluid Mech.* **208**, 509–543 (1989).
- C. R. Williams, M. A. Bees, A tale of three taxes: Photo-gyro-gravitactic bioconvection. *J. Exp. Biol.* **214**, 2398–2408 (2011).
- P. Berthold *et al.*, Channelrhodopsin-1 initiates phototaxis and photophobic responses in *Chlamydomonas* by immediate light-induced depolarization. *Plant Cell* **20**, 1665–1677 (2008).
- C. T. Kreis, M. Le Blay, C. Linne, M. M. Makowski, O. Bäumchen, Adhesion of *Chlamydomonas* microalgae to surfaces is switchable by light. *Nat. Phys.* **14**, 45–49 (2018).
- A. Hemscheier *et al.*, Copper response regulator1-dependent and-independent responses of the *Chlamydomonas reinhardtii* transcriptome to dark anoxia. *Plant Cell* **25**, 3186–3211 (2013).
- T. J. Pedley, N. Hill, J. O. Kessler, The growth of bioconvection patterns in a uniform suspension of gyrotactic micro-organisms. *J. Fluid Mech.* **195**, 223–237 (1988).
- R. J. Adrian, J. Westerweel, *Particle Image Velocimetry* (Cambridge University Press, 2011), vol. 30.
- J. O. Kessler, Hydrodynamic focusing of motile algal cells. *Nature* **313**, 218–220 (1985).
- M. Polin, I. Tuval, K. Drescher, J. P. Gollub, R. E. Goldstein, *Chlamydomonas* swims with two "gears" in a eukaryotic version of run-and-tumble locomotion. *Science* **325**, 487–490 (2009).
- L. Caprini, U. M. B. Marconi, Time-dependent properties of interacting active matter: Dynamical behavior of one-dimensional systems of self-propelled particles. *Phys. Rev. Res.* **2**, 033518 (2020).
- A. Ramamonjy, P. Brunet, J. Dervaux, Pattern formation in photo-controlled bioconvection. *J. Fluid Mech.* **971**, A29 (2023).
- É. Fodor, M. C. Marchetti, The statistical physics of active matter: From self-catalytic colloids to living cells. *Phys. A Stat. Mech. Appl.* **504**, 106–120 (2018).
- E. H. Harris, D. B. Stern, G. B. Witman, Eds., "Chapter 2 - cell architecture" in *The Chlamydomonas Sourcebook (Second Edition)* (Academic Press, London, ed. 2, 2009), pp. 25–64.
- F. Rühle, E. Stark, Emergent collective dynamics of bottom-heavy squirmers under gravity. *Eur. Phys. J. E* **43**, 1–17 (2020).
- A. Kage, C. Hosoya, S. A. Baba, Y. Mogami, Drastic reorganization of the bioconvection pattern of *Chlamydomonas*: Quantitative analysis of the pattern transition response. *J. Exp. Biol.* **216**, 4557–4566 (2013).
- R. E. Catalan *et al.*, Light-regulated adsorption and desorption of *Chlamydomonas* cells at surfaces. *Soft Matter* **19**, 306–314 (2023).
- H. Yuen, J. Princen, J. Illingworth, J. Kittler, Comparative study of hough transform methods for circle finding. *Image Vis. Comput.* **8**, 71–77 (1990).
- D. Blair, E. Dufresne, The Matlab particle tracking code repository. Matlab. <http://physics.georgetown.edu/matlab/>. Accessed 1 March 2020.
- D. A. Lyon, The discrete fourier transform, Part 4: Spectral leakage. *J. Object Technol.* **8**, 23–34 (2009).
- J. I. Jackson, C. H. Meyer, D. G. Nishimura, A. Macovski, Selection of a convolution function for fourier inversion using gridding (computerised tomography application). *IEEE Trans. Med. Imaging* **10**, 473–478 (1991).
- W. Thielicke, R. Sonntag, Particle image velocimetry for MATLAB: Accuracy and enhanced algorithms in PIVlab. *J. Open Res. Softw.* **9**, 12 (2021).
- A. M. Reza, Realization of the contrast limited adaptive histogram equalization (CLAHE) for real-time image enhancement. *J. VLSI Sig. Proc. Syst.* **38**, 35–44 (2004).
- W. Blanken, P. R. Postma, L. de Winter, R. H. Wijffels, M. Janssen, Predicting microalgae growth. *Algal Res.* **14**, 28–38 (2016).
- J. A. Myers, B. S. Curtis, W. R. Curtis, Improving accuracy of cell and chromophore concentration measurements using optical density. *BMC Biophys.* **6**, 1–16 (2013).
- J. J. Lamb, G. Røkke, M. F. Hohmann-Marriott, Chlorophyll fluorescence emission spectroscopy of oxygenic organisms at 77 K. *Photosynthetica* **56**, 105–124 (2018).
- A. Fragkopoulou, O. Bäumchen, F. Böhme, N. Drewes, Metabolically controlled bioconvection with *C. reinhardtii*-Experimental data. Zenodo. <https://doi.org/10.5281/zenodo.14517920>. Deposited 18 December 2024.